Nanoscale

Accepted Manuscript

This article can be cited before page numbers have been issued, to do this please use: H. A. Girard, M. Finas, L. Saoudi, F. Ducrozet, M. BRIANT, O. Sublemontier, A. Milosavljevic, C. Nicolas and J. C. Arnault, *Nanoscale*, 2025, DOI: 10.1039/D5NR02241J.

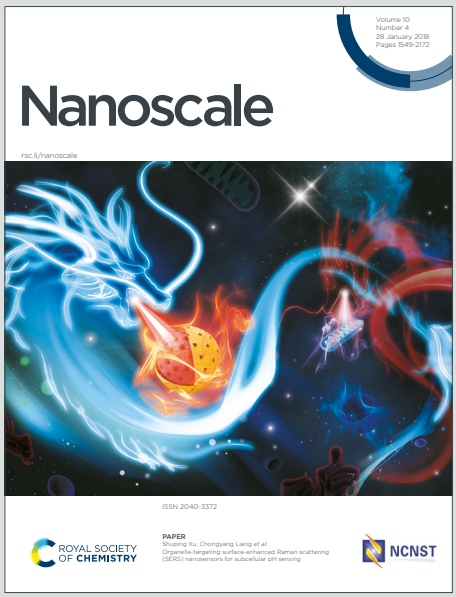

ROYAL SOCIETY OF CHEMISTRY

rsc.li/nanoscale

Chemistry of the shallow surface of isolated nanodiamonds probed by synchrotron X-ray photoemission

View Article Online
DOI: 10.1039/D5NR02241J

H.A. Girard[a], M. Finas[a], L. Saoudi[a], F. Ducrozet[a,b], M. Briant[a], O. Sublemontier[a], A. R. Milosavljević[c], C. Nicolas[c], J.-C. Arnault[a]

[a] Université Paris-Saclay, CEA, CNRS, NIMBE, 91191 Gif sur Yvette, France

[b] Institut de Chimie Physique, Université Paris-Saclay – CNRS, UMR 8000, 91405 Orsay, France

[c] Synchrotron SOLEIL, L'Orme des Merisiers Départementale 128, 91190 Saint-Aubin, France

Abstract

Nanodiamonds (ND) are under active investigation for their unique properties and potential applications in energy, quantum technologies, and nanomedicine. The surface chemistry of ND significantly influences their semiconducting behavior, colloidal properties, and interactions with water and light. To gain deeper insights into these properties, this study employs synchrotron X-ray photoelectron spectroscopy (XPS) to investigate the shallow surface chemistry of isolated nanodiamonds in an aerodynamic jet. Employing a photon energy of 360 eV, we probed the surface of nanodiamonds with a depth of 0.3 nm. Based on the collected data, the band diagrams of the particles have been established, reporting the expected differences in electron affinity between the two surface chemistries. Interestingly, both Ox-MND and H-MND showed fairly similar C1s core level signatures, a phenomenon discussed in detail within the article, including the effect of residual water molecules. This raises important questions about the true interface formed with water molecules when ND are in aqueous suspension, particularly in the context of their use as photocatalysts.

1. Introduction

Nanoscale diamond particles, i.e. nanodiamonds (ND), are currently under active investigation for their valuable and combinable properties in the fields of energy, quantum applications and nanomedicine [1–3]. Nanodiamond inherits most of the outstanding properties of bulk diamond, in particular its semiconducting behavior for which surface chemistry plays a key role[4]. For instance, the diamond lattice linked to hydrogen atoms confers to hydrogenated nanodiamond (H-ND) a negative electron affinity (NEA), whereas oxygenated terminations (Ox-ND) lead to a positive electron affinity (PEA)[5]. The corresponding band diagram of hydrogenated nanodiamond thus favors the emission of highly reducing solvated electrons under UV illumination, which have been successfully used for CO_2 or N_2 photocatalytic reduction [6,7] and more recently for pollutant degradation [8,9]. A p-type conductivity can also be obtained at the H-ND surface via interactions with adsorbates that act as electron acceptors through surface transfer doping [5,10,11]. The related electrical conductivity was measured for hydrogenated nanodiamonds of different natures and sizes [12]. Apart from influencing semiconducting properties, tuning the surface termination of nanodiamonds will also affects their colloidal behavior. ND can be stabilized in water for months without any surfactant, but H-ND and Ox-ND aqueous suspensions will exhibit opposite surface charges with positive and negative zeta potentials at neutral pH, respectively [13]. If the cause of the negatively charged Ox-ND is well known (deprotonation of carboxyl groups), the origin of the positive charge of H-ND is still debated. Spectroscopic approaches [14,15] evidenced that surface chemistry influences the spatial arrangement of water molecules surrounding ND. For H-ND, these works suggested a long-range disruption of the water hydrogen bonds network.

View Article Online
DOI: 10.1039/D5NR02241J

Still regarding the influence of surface chemistry on ND physico-chemical properties, specific behaviors were observed considering light-matter interactions. For instance, aqueous colloids of hydrogenated nanodiamonds exposed to gamma or X-ray irradiations revealed unusual overproduction of hydroxyl radicals and/or solvated electrons compared to water radiolysis standards[16,17,18], not reproduced on Ox-ND. On the opposite, photocatalytic hydrogen production via water splitting under visible light was only reported for oxidized ND suspended in water[19]. The mechanisms involved in hydrogen production, including those taking place at the ND/water interface, are still unclear but are clearly specific to the oxidized surface.

Thus, to shed light upon these specific properties of ND in water according to their surface terminations, an investigation of their shallow surface chemistry is required to appreciate the real interface formed with water molecules when ND are in colloidal suspension. In that sense, X-ray photoelectron spectroscopy (XPS) appears to be an appropriate technique to study the surface chemistry of nanodiamonds[20]. Nevertheless, as the dimensions of the nanoparticles approach the inelastic mean free path (IMFP) of the generated photoelectrons (which is a few nanometers in diamond), conventional XPS data must be carefully analyzed to account for so-called “nano-effects”: the signal from the surface may become predominant depending on the size of the nanoparticle. [21–23]. To mitigate this effect, smaller IMFP should be considered, as previously performed on bulk diamond [24,25]. Another limitation of conventional XPS is the deposition of nanoparticles on a substrate. Depending on the contact between the nanodiamonds (ND) and the underlying layer, inhomogeneous surface charging can occur during analysis, which can distort both the appearance of the core levels photoemission peaks and their binding energy positions. This aspect is particularly crucial when comparing hydrogenated ND, which are conductive [11], with oxidized ND, which are highly insulating.

In this context, this article aims to describe XPS analysis performed on a jet of isolated (or slightly aggregated) nanodiamonds, directly produced from an aqueous colloid through a nebulizer and an aerodynamic lens [26,27]. Using a synchrotron photon beam that intersects the jet of nanoparticles, photo-electrons coming from isolated ND were then analyzed in energy. To probe the shallow surface of the nanoparticles, a photon energy of 360 eV was used, unless specified otherwise, which corresponds to an inelastic mean free path (IMFP) estimated to 0.3-0.5 nm for C1s electrons in diamond[28,29]. By employing a particle jet instead of a substrate deposit, it was thus possible to circumvent charging effects. In this study, we focused on the surface chemistry of hydrogenated and oxidized nanodiamonds synthesized through a milling process[30], as their electronic properties closely resemble those of bulk diamond.

2. Results

The XPS analyses presented below were realized on milled nanodiamonds (MND) that were oxidized (Ox-MND) or hydrogenated (H-MND) in gas phase at high temperature, following procedures detailed in our previous studies[10,11]. Thus, for complete characterization of these H-MND and Ox-MND, including dynamic light scattering experiments and infrared or Raman spectroscopies, please refer to our previous paper[10].

a) Hydrogenated MND

View Article Online
DOI: 10.1039/D5NR02241J

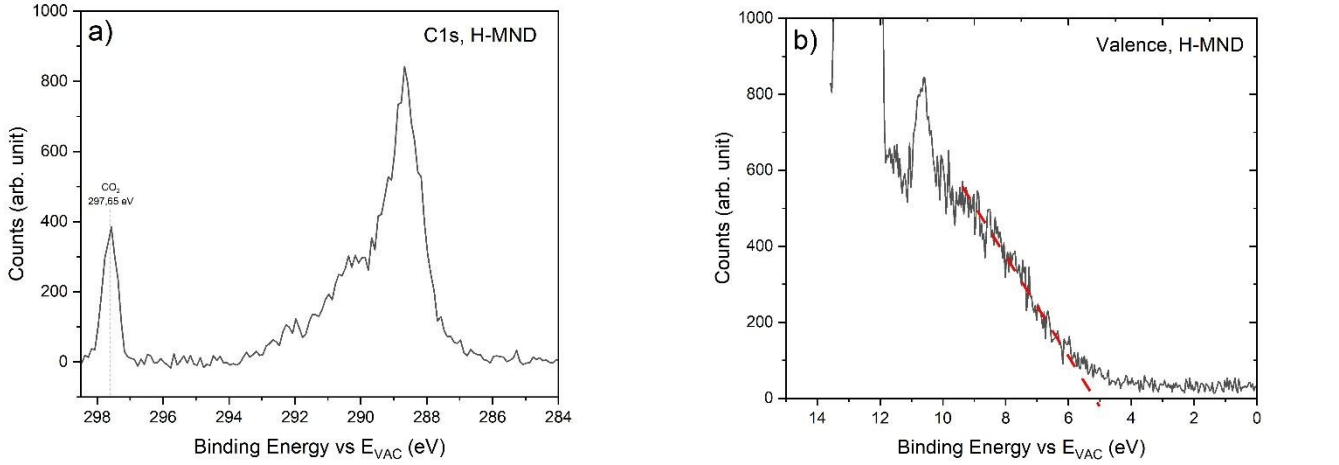

Figure 1 Photoelectron spectra of hydrogenated milled ND (a) C1s spectrum recorded with a photon energy of 360 eV, (b) Valence band spectrum recorded with a photon energy of 100 eV. At photon energies of 360 eV and 100 eV, the overall resolutions in the XPS spectra are 0.39 and 0.11 eV respectively. Binding energies are referenced to the vacuum level defined with CO_2 gas.

Figure 1 (a) shows the C1s XPS of H-MND recorded for a photon energy of 360 eV. Binding energies are referenced here to the vacuum level defined with CO_2 gas introduced into the UHV chamber which serves as reference (E_B=297.65 eV)[31]. In these conditions, the C1s peak maximum of the H-MND nanoparticles is located at 288.6 eV.

In order to gain further insight into this spectrum, deconvolution and assignment of the components is mandatory, but it is important to keep in mind that at this photon energy, only the very first atomic layers are probed. There is currently no assurance that the predominant peak aligns with the signature of diamond C-C sp^3 bonds, which would allow the attribution of the others peaks. A comparative analysis with a C1s spectrum recorded on a conventional spectrometer, i.e. a standard laboratory spectrometer equipped with a monochromatic Al Kα (1486.6 eV) X-ray source is thus proposed. However, a straightforward comparison of both C1s is impossible, as the binding energies obtained on a conventional spectrometer are referenced to the Fermi level of the material (E_F), whereas in the experiments carried out with the synchrotron beam on the nanoparticle jet, the energies are referenced to E_{VAC} given by the isolated CO_2 molecules which serve as reference (see methods part) (Figure 2 (a)). Note that on our nanoparticles, it would be more appropriate to consider a near-surface vacuum level, which corresponds to the energy level of an electron with zero kinetic energy relative to the sample surface ($E_{VAC}(s)$), distinct from the vacuum level at infinity ($E_{VAC}(\infty)$), which represents the energy of an electron at rest far from the solid surface [32]. In XPS/UPS measurements, this ($E_{VAC}(s)$) should be considered to build a band diagram. However, due to the specificity of the measurement performed here, conducted on isolated particles which are not in contact with a substrate, this local vacuum level cannot be strictly define, only the ($E_{VAC}(\infty)$) derived from CO_2 gas is available.

To overcome this issue, referring both C1s spectra to the maximum of the valence band (E_{VBM}) would allow reliable comparison. Figure 1 (b) shows the valence band spectrum recorded on H-MND with the synchrotron beam, referenced to E_{VAC} derived from CO_2 gas. A maximum of the valence band at 5.1 eV is measured. With a conventional XPS approach, a value of 1.1 eV vs. E_F was previously measured on similar H-MND [10]. According to these values, a simplified band diagram is proposed in Figure 2 (a). Thanks to the synchrotron measurements, the valence band maximum of the H-MND can be positioned at 5.1 eV below E_{VAC}. From conventional XPS results, the Fermi level of the material (E_F) can be positioned at 1.1 eV above the valence band maximum. C1s maximum of conventional and synchrotron measurements can then be reported, at 284.8 eV vs. E_F and 288.6 eV vs. E_{VAC} respectively. By adopting the valence band maximum (E_{VBM}) as a new common reference, it appears that the two C1s maxima are nearly identical, both positioned at 283.6 eV, within the

View Article Online
DOI: 10.1039/D5NR02241J

margin of the experimental error. This simplified band diagram further evidences that, if we consider a band gap of 5.4 eV previously measured by reflection electron energy loss spectroscopy (REELS) on the same nanoparticles [11], a similar negative electron affinity (0.3 eV) than the one measured by UPS in earlier reports [5,11]. This would evidence that the vacuum level derived from the calibration gas is close to the local Evac of the nanoparticles, within the margin of the experimental error.

The C1s spectra obtained on the synchrotron and the conventional spectrometers are shown in Figure 2 (b), both referenced to the E_{VBM}. Note that the energy resolution of the conventional spectrometer for a C1s spectrum in our analysis conditions is around 0.35 eV, which is in the same order of magnitude as the one for synchrotron XPS. This allows the comparison made here.

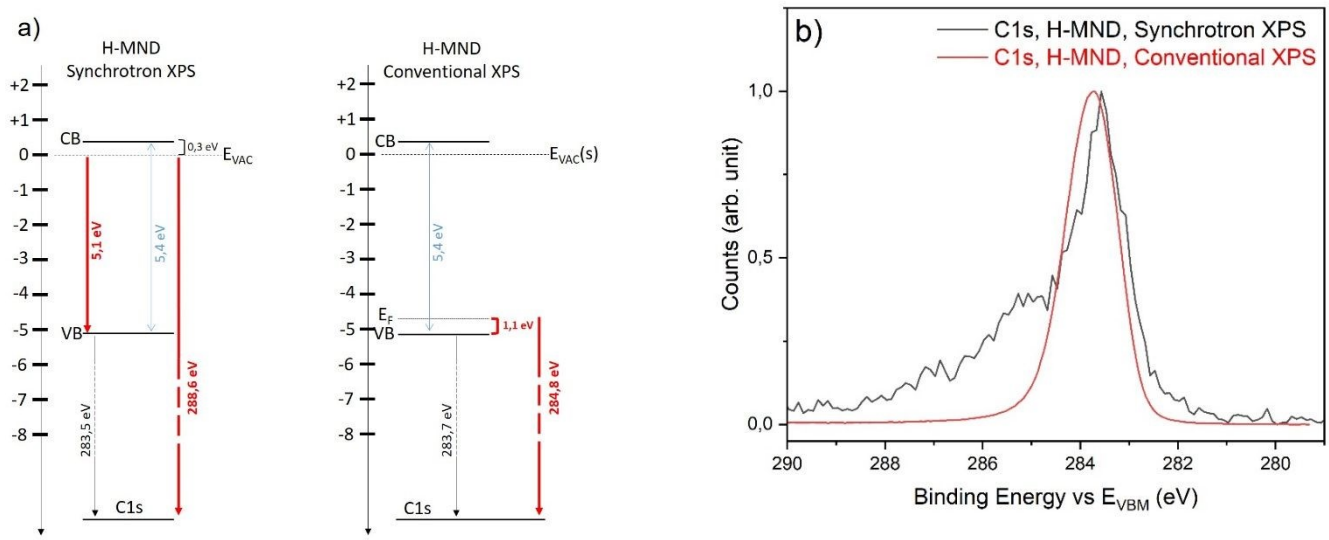

Figure 2 (a) Simplified band diagrams of H-MND built from synchrotron and conventional XPS measurements (in red) and values from literature (in blue) and (b) C1s spectra of H-MND recorded on synchrotron and on conventional XPS. Spectra are normalized to the main contribution. Binding energies are referenced to E_{VBM}.

Considering the agreement in the position of the C1s peak and the similar energy resolutions of the two spectrometers, we thus applied to both spectra the fitting parameters previously reported for the conventional XPS analysis [10]. Fitted spectra are presented on Figure 3. The position and relative area of each contribution are reported in the Table 1.

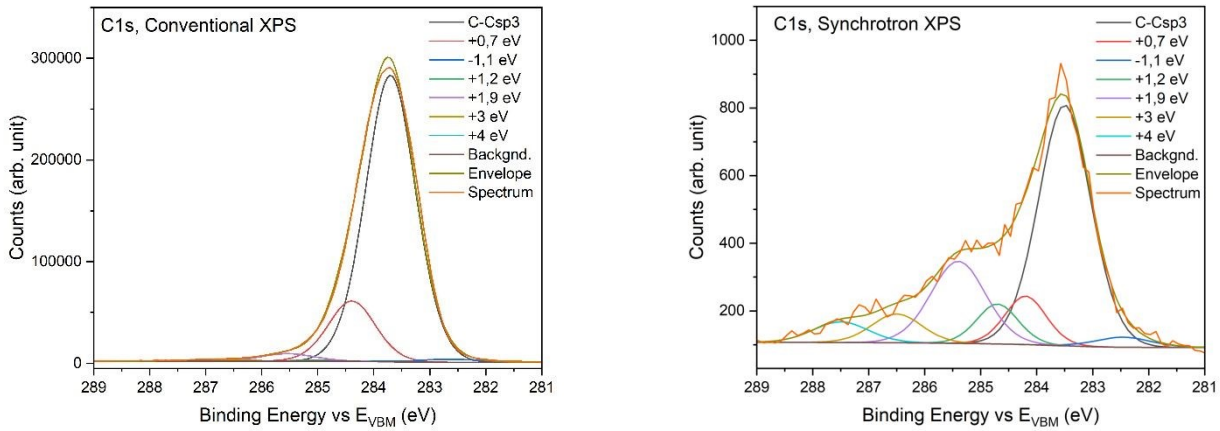

Figure 3 C1s fitted spectra of H-MND recorded on a conventional and on the synchrotron XPS. Binding energies are referenced to E_{VBM}.

View Article Online
DOI: 10.1039/D5NR02241J

Assignments	Energy shift (eV)	Conv. XPS C1s relative area (%)	Synch. XPS C1s relative area (%)
C=C sp²	- 1.1 eV	1.0	2.3
C-C sp³	C-C sp³	79.9	52.9
C-C defects	+ 0.7 eV	15.9	8.4
C-OH	+ 1.2 eV	0.3	6.9
C-O-C	+ 1.9 eV	2.2	18.9
C=O	+ 3 eV	0.6	6.0
COOH	+ 4 eV	0.1	4.6

Table 1 Details of the different contributions of H-MND fitted C1s and their relative area (in %) for conventional and synchrotron XPS.

In both cases, the main peak corresponds to the C-C sp³ bonds of diamond. The second contribution at higher binding energy (+ 0.7 eV) can be assigned to defective C-C sp³ bonds, including core and surface defects of the diamond lattice, as well as sp³ carbons in the vicinity of surface terminations. It is important to highlight here that hydrogenated surface terminations, i.e. surface carbon atoms saturated with one or several hydrogen atoms, will not be directly visible by XPS but their presence will contribute to this defective C-C component[33,34]. The four others at higher binding energies are related to oxygen functional groups with C-OH, C-O-C, C=O and COOH bonds at + 1.2, + 1.9, + 3 and + 4 eV, respectively [10,35]. The peak recorded at lower binding energy (- 1.1 eV) corresponds to sp² carbon.

As the shallow surface is highly overexpressed with synchrotron XPS, we can note a significant decrease of the "bulk" contributions, the C-C sp³ and the one related to defects, from 80% to 53% and from 16% to 8%, respectively. At the same time, contributions related to functional oxygen groups are all enhanced, from 3% to 37% in total. The important proportion of carbon-oxygen functions at the surface of H-MND will be discussed later on.

Considering the peak related to sp² carbon, the contributions measured at 360 eV (synchrotron XPS) and 1486 eV (conventional XPS) remain very close and very limited (< 2.5 % of the total C1s area). Such bonds may result from local reconstructions of unsaturated carbon bonds after the hydrogenation gas treatment [35]. However, given that this component is related to the surface of the nanoparticle, it is surprising that it has not increased when lowering the photon energy.

b) Oxidized-MND

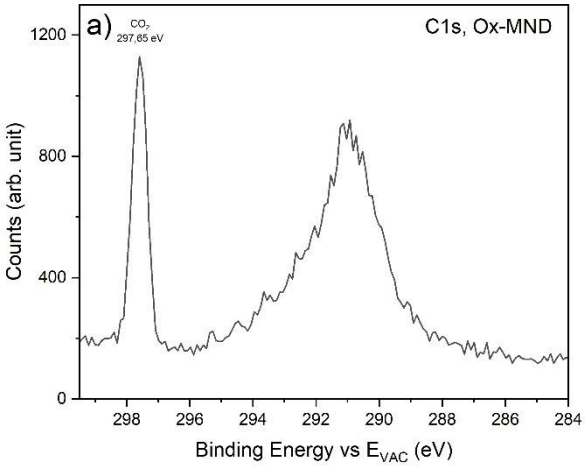

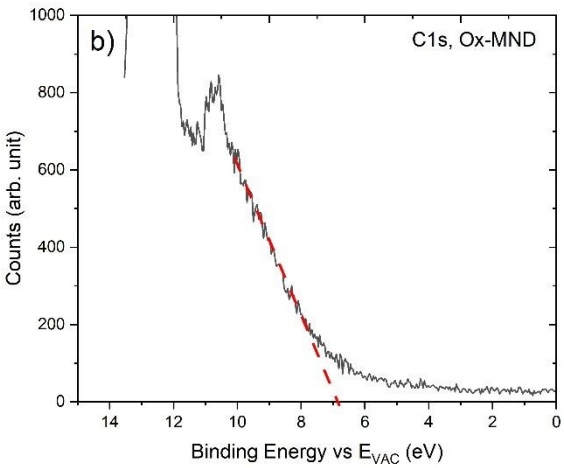

View Article Online
DOI: 10.1039/D5NR02241J

Figure 4 (a) C1s spectrum of oxidized milled ND (Ox-MND) and CO_2 reference recorded with a photon energy of 360 eV. (b) Valence band spectrum of Ox-MND recorded with a photon energy of 100 eV. Binding energies are referenced to the vacuum level defined with CO_2 gas.

For Ox-MND, the C1s maximum is located at 291 eV with a FWHM of 2 eV (Figure 4 (a)). This peak appears significantly wider than the one obtained for H-MND (Figure 1). Figure 4 (b) shows the valence band spectrum recorded on Ox-MND with a maximum at 6.9 eV vs E_{VAC}. With a conventional XPS approach, a value of 3.4 eV vs. the Fermi level (E_F) was previously measured on similar Ox-MND [10]. Consequently, a band diagram built from these information is shown in Figure 5 (a). Here, 0.4 eV of difference is expected between the C1s maxima recorded on the synchrotron and on the conventional spectrometers. These band diagrams also reveal a positive electron affinity (PEA) of 1.5 eV, which is expected for Ox-MND [5,11].

As for H-MND, conventional and synchrotron XPS spectra were rescaled to the E_{VBM} and are displayed on Figure 5 (b).

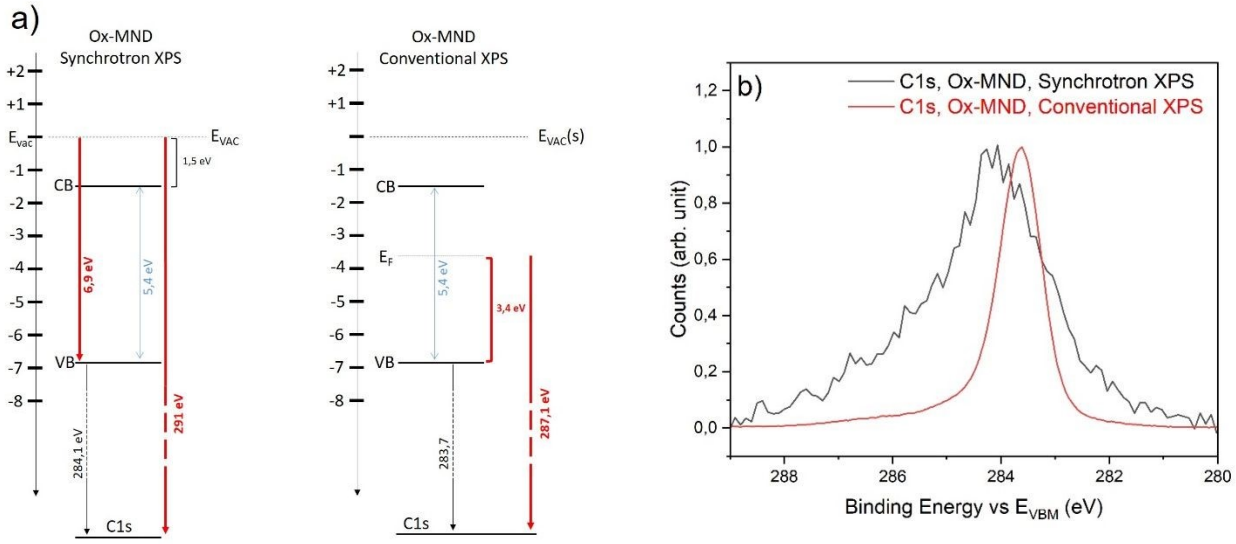

Figure 5 (a) Simplified band diagrams of Ox-MND built from synchrotron and conventional XPS measurements (in red) and values from literature (in blue) and (b) C1s spectra of Ox-MND recorded on synchrotron and on conventional XPS. Spectra are normalized in intensity to the main carbon contribution. Binding energies are referenced to E_{VBM}.

We applied to both spectra the fitting previously reported for conventional XPS analysis[10]. Fitted spectra are presented on Figure 6. The position and relative area of each contribution are reported in the Table 2.

View Article Online
DOI: 10.1039/D5NR02241J

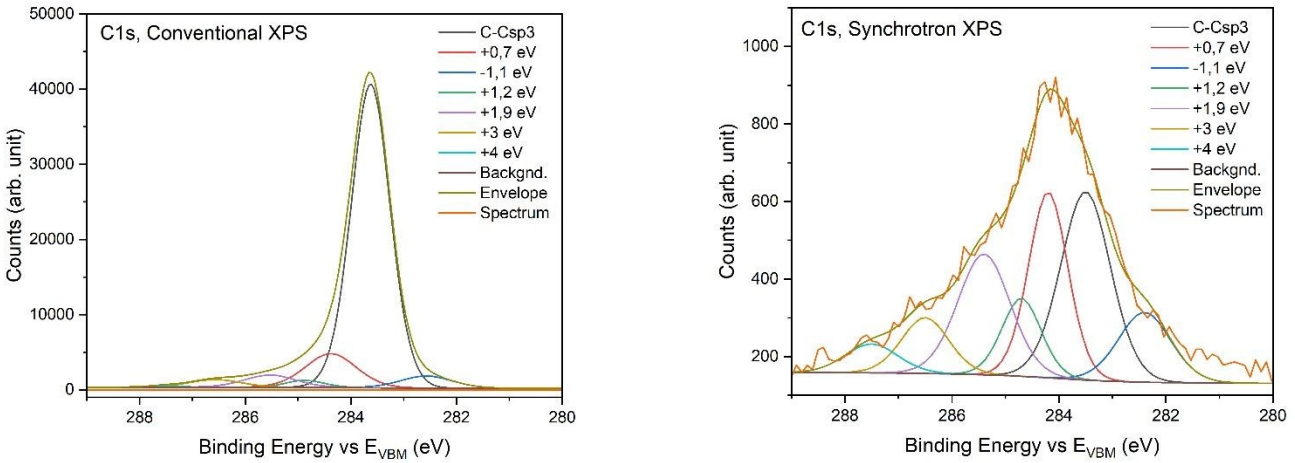

Figure 6 C1s fitted spectra of Ox-MND recorded on a conventional XPS and on the synchrotron XPS. Binding energies are referenced to E_{VBM}.

Assignments	Energy shift (eV)	Conv. XPS C1s relative area (%)	Synch. XPS C1s relative area (%)
C=C sp²	- 1.1 eV	4.0	10.7
C-C sp³	C-C sp³	76.1	27.9
C-C defects	+ 0.7 eV	11.1	21.4
C-OH	+ 1.2 eV	1.7	9.0
C-O-C	+ 1.9 eV	4.1	18.7
C=O	+ 3 eV	2.6	7.8
COOH	+ 4 eV	0.4	4.5

Table 2 Details of the different contributions of Ox-MND fitted C1s and their relative area (in %) for conventional and synchrotron XPS.

As the shallow surface is highly preferentially probed at 360 eV (synchrotron), we can note a significant decrease of the C-C sp³ bulk contribution from 76% to 28%. As for H-MND, all contributions related to carbon-oxygen groups are enhanced: from 9% to 40% in total. The C-C sp² contribution underwent a significant increase from 4% to 11% of the total C1s area. For Ox-MND, the contribution related to defects (+ 0.7 eV vs C-C sp³) is exalted from 11 to 21%. This would suggest a higher density of defects at the surface compared to H-MND (in agreement with HRTEM observations [10]).

3. Discussion

In recent years, there has been a growing interest in nanodiamonds produced by milling (MND), particularly regarding their surface chemistry, electronic properties, and colloidal behavior. The prevailing consensus is that these MND exhibit significant similarities to bulk diamond, especially in their surface chemistry and electronic properties. This originates from their excellent crystalline quality. For instance, IR, Raman and photo-electron spectroscopies of Ox-MND show an oxidized chemistry composed of alcohols, ethers, carbonyls and carboxyls, similar to that seen for bulk diamond [7,10,36,37]. It should be noted that a residual sp² carbon is also generally measured on these Ox-MND. In contrast, H-MND, which is typically obtained by annealing Ox-MND under H_2 at temperatures higher than 700°C [7,10,36], exhibits a nearly complete desorption of oxidized functions, accompanied by a decrease in sp² carbon [10,36]. In a similar manner to bulk hydrogenated diamond, a surface conductivity has been demonstrated by several research groups on these H-MND, either indirectly by infrared

View Article Online
DOI: 10.1039/D5NR02241J

spectroscopy via Fano-type destructive interferences [36,38,39] or more directly by conductivity measurements [12]. Recent UPS/XPS studies conducted by our team have also revealed that this conductivity is likely assigned to adsorbates originating from air and/or water, which induce a pseudo p-type behavior via a charge transfer mechanism [11]. Furthermore, we have demonstrated the feasibility of inducing and removing this pseudo p-type doping by exposing the sample to vacuum annealing and re-exposure to water/air.

However, most of the spectroscopic studies cited above that have been used in recent years to investigate chemical and semiconducting properties of H-MND and Ox-MND were carried out on nanoparticles that were drop-casted or spin-coated on a substrate from a colloidal suspension. This methodological approach, mandatory for analyzing nanoparticles with conventional tools, may not accurately reflect the surface chemistry of nanodiamonds as they exist in colloids. Depositing a drop of solvent containing nanoparticles and then allowing it to dry can potentially alter their surface chemistry, particularly with regard to adsorbates, as well as promoting strong interactions with the substrate during spectroscopic measurements [40]. Finally, with specific regard to XPS, it is important to remember that while this technique is rightly considered as a surface analysis for bulk materials, it differs at the scale of nanometric particles. As briefly mentioned in the introduction, at the energies usually employed in laboratory spectrometers (Al Kα 1486.6 eV), electron escape depths are of the order of a few nanometers for diamond [29]. Given the wide size distribution of MND [41], which ranges from a few nanometers to a few dozen, collected photoelectrons may originate either from the core for the smallest nanoparticles or from the surface for the largest nanoparticles. Additionally, for the smallest nanoparticles (< 10 nm), an enhancement of the surface contribution may also arise, as clearly established by Baer et al.[21].

The results presented here have therefore the advantage of being truly “surface sensitive”, even at the scale of nanoparticles, since we probe mostly 0.3-0.5 nm beneath the surface. Furthermore, this approach by jet allows the nanoparticles to statistically receive not more than one photon each[42], thus X-ray induced surface modification can be avoided, thereby ensuring even more reliable results. Therefore, we have access to the real signature of the surface chemistry of MND, as close as possible to what they are in colloids, with no risk of distortion of the XPS spectra due to interaction with a substrate, a charging effect or even in situ modification under X-rays.

Considering all these factors, we can now compare accurately the surface chemistries of H-MND and Ox-MND. For Ox-MND, an enhancement of surface-related functions (carbon-oxygen groups and sp^2 carbon) and sub-surface functions (defective sp^3 C-C bonds) is observed compared to conventional XPS analysis, with a concomitant reduction of the core component (C-C sp^3). This finding is consistent with prior studies employing energy-resolved XPS on bulk diamond, which demonstrated an enhancement of surface components for photon energies close to 360 eV [24,43]. In their study, Chemin et al. reported a C1s core level of oxidized bulk diamond recorded with a photon energy of 335 eV (IMFP ≈ 0.6 nm), where the core component accounted for approximately 60% of the total carbon, without distinguishing between C-C sp^3 and defective sp^3 C-C bonds. Here, the combined contribution of C-C sp^3 and defective sp^3 C-C bonds reaches nearly 50% of the carbon, which is comparable.

In contrast, the surface analysis of H-MND presents a more challenging aspect to address. Compared to Ox-MND, the C-C sp^3 component constitutes the majority of the relative area in relation to the surface-related components. This is due to the reduced presence of defective C-C bonds and sp^2 carbon bonds. This observation aligns with previous reports where annealing under H_2 of oxidized surfaces has been shown to “heal” the surface defects and remove residual sp^2 carbon [10,35].

View Article Online
DOI: 10.1039/D5NR02241J

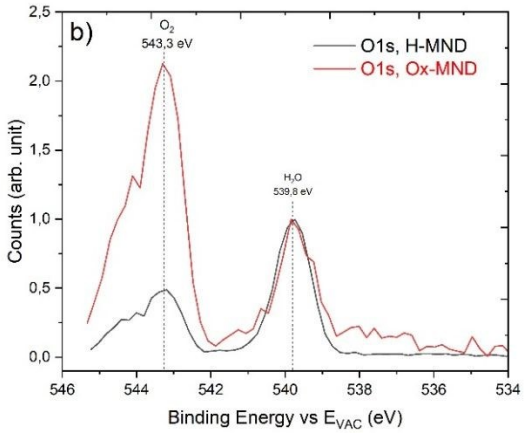

Figure 7 O1s spectra of H-MND and Ox-MND recorded at 600 eV, referred to E_{VAC}. Spectra are normalized to the 539.8 eV peak. O_2 gas was introduced into the UHV chamber as a binding energy reference (543.3 eV) [44].

Another notable finding is the presence of "carbon-oxygen" related groups (from + 1.2 to + 4 eV) on H-MND C1s spectrum, with proportions nearly identical to those observed for Ox-MND (37% of the overall C1s for H-MND versus 40% for Ox-MND). Examining the O1s spectra recorded on H-MND and Ox-MND in Figure 7, it appears that both MND are covered with a water layer (539.8 eV), with no obvious other contributions. Note that due to the geometry of the system, we can ensure that this XPS signal is related to the surface of nanodiamonds and is not originating from the carrier gas and the residual solvent [45]. While these O1s spectra do not provide information about O-C components, which should be hidden by the water signature, they do highlight the high affinity of H-MND for water.

The origin of these apparent C-O and C=O signatures on H-MND C1s core level is a crucial aspect to investigate. IR spectroscopy and conventional XPS highlight clear differences in surface chemistries between H-MND and Ox-MND, as revealed in our previous study on nanodiamonds prepared under identical conditions[10]. Briefly, Ox-MND contain over 9 at.% oxygen, as measured by conventional XPS, with strong C=O stretching modes in their IR spectrum. In contrast, H-MND exhibit only 1 at.% oxygen, showing in their IR spectrum a near-complete disappearance of C=O modes, replaced by strong C-H stretching modes. However, these techniques either analyze the entire nanoparticle (IR) or account for a variable portion of the core (XPS, as explained above). As a result, the surface chemistry may be masked by contributions from sub-surface or core regions, which are revealed at the scale examined in this study. Nevertheless, if the H-MND surface was truly oxidized, with a similar proportion of oxidized terminations as on Ox-MND, it would contradict the electron affinity measurements. These measurements show a clear shift from positive for Ox-MND (+ 1.5 eV) to negative for H-MND (- 0.3 eV), as determined from the position of the valence band maximum E_{VBM}[10]. It is therefore obvious that there is an apparent incoherence between equivalent proportions of C-O/C=O terminations as measured on C1s spectra of Ox-MND and H-MND, while two clearly distinct signs and values of the electron affinity are simultaneously observed. As recently reviewed by Hamers' team, the negative electron affinity (NEA) is directly linked to the presence of H-terminations and the associated $C^{\delta-}$-$H^{\delta+}$ surface dipoles, while the positive electron affinity is linked to oxidized terminations ($C^{\delta+}$-$O^{\delta-}$) [24]. Therefore, two diamond materials evidencing such different electron affinities (in signs and values) should exhibit very significant differences in terms of carbon-oxygen functions proportion at their surface[46].

View Article Online
DOI: 10.1039/D5NR02241J

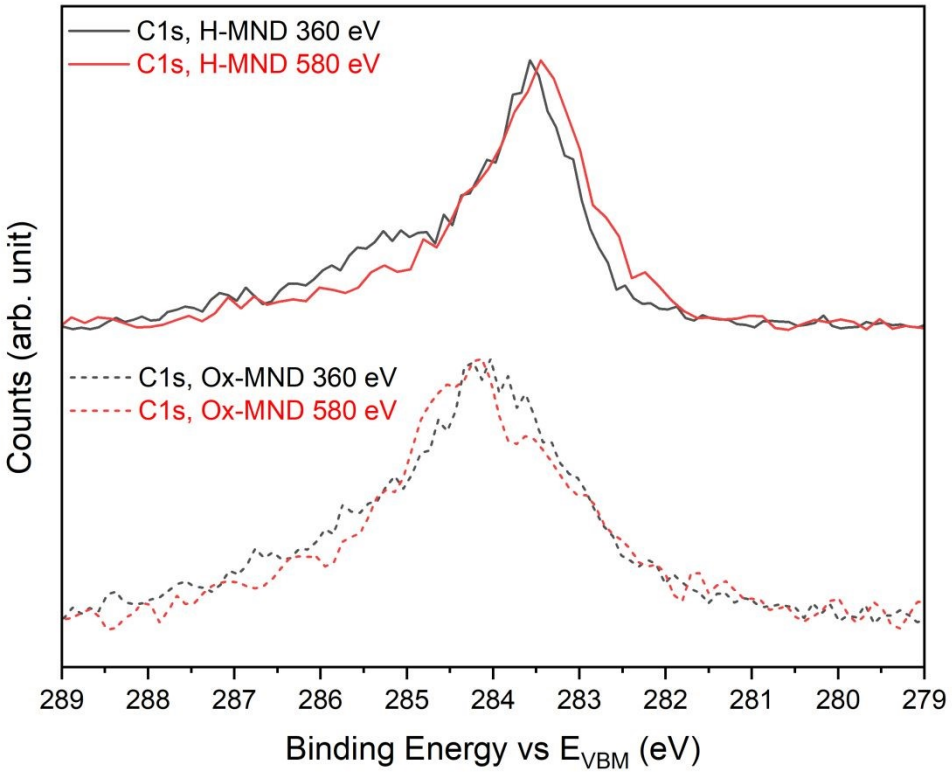

Figure 8 C1s spectra of H-MND and Ox-MND recorded at 360 eV and 580 eV, spectra normalized to the main contribution. Binding energies are referenced to E_{VBM}.

At this stage, only hypotheses can be advanced to clarify this apparent contradiction. One can assume first a different spatial location of C-O bonds at both MND surfaces, within the first nanometer of the nanoparticles. Such oxygen functional groups may be present at the surface for H-MND, while it may be partially covered by the more abundant sp^2 carbon for Ox-MND (Table 2). Such hypothesis may lead to an underestimation of C-O bonds for the oxidized surface in the present XPS analysis which mainly probes the shallow surface at 360 eV. This hypothesis would explain the different evolutions of carbon-oxygen contributions for a higher probed depth (at 580 eV): a clear decrease for H-MND (Figure 8) and an unchanged signal for Ox-MND (Figure 8). However, for MND, we have no other experimental evidence to support such surface structuring.

Another possibility would be to consider that C-O and C=O components may not be linked to carbon-oxygen groups covalently bonded to MND surface, but may originate from some species adsorbed on their surface, which would not affect the NEA. This postulate is supported by the C1s spectrum recorded at a higher photon energy of 580 eV on H-MND, which allows to probe a little deeper into the particle (up to 0.6 nm). As shown in Figure 8 (a), the shoulder at 290.5 eV, which would correspond to the signature of these species adsorbed on the H-MND surface, is less pronounced at higher photon energies. At this stage, it is important to remind that these experiments reflect as closely as possible the state of the nanoparticles as they are in the colloid, without any interaction with a substrate. In the present experiments, nanoparticles are nebulized from the colloid a few fractions of a second before being analyzed, and they only dry for a very short time. As a matter of fact, they remain surrounded by a thin water layer during the analysis, as shown by the O1s spectrum (Figure 7) on which water signature is clearly visible at 539.8 eV [44]. This water layer lying at the surface of H-MND may also participate to the significant presence of C-O/C=O terminations on their surface. Over the last two decades, numerous theoretical and experimental studies have explored the spontaneous interactions between water and hydrogenated bulk diamond surfaces[47–49]. These studies suggest that the dissociation of water molecules is likely to occur

View Article Online
DOI: 10.1039/D5NR02241J

on both hydrogenated and bare diamond surfaces, a process facilitated by carbon dimers and dangling bonds. In some cases, the dissociation of water molecules on a diamond surface can result in the formation of weakly bounded carbonyl and alcohol groups[48]. The observed phenomenon may involve the formation of weakly bound C-O/C=O terminations upon contact with water, potentially located on dangling bonds and reconstructed surfaces, while the negative electron affinity due to the C-H terminations remains preserved. It should be noted that in Chemin et al.[43] the C1s core levels of hydrogenated bulk diamond surfaces, also characterized using a photon energy of 335 eV, do not exhibit such C-O and C=O functionalities. This is likely because a water layer is not expected to be preserved in these experiments, which are performed under ultra-high vacuum conditions and on surfaces that have only been exposed to ambient air beforehand.

Addressing the potential existence of a chemical compound lying at the surface of the H-MND, it is also essential to consider recent research works that have revealed their surface conductivity [10,12,38,39] and the pseudo p-type doping that we measured by UPS experiments on the same H-MND [11] and which was also reported for equivalent material by Milaieva et al. [5]. This pseudo p-type doping originates from a transfer doping mechanism, which requires the presence of electron acceptors located at the surface. In the context of bulk diamond, molecular species such as O_3, NO_2, NO, and SO_2 have been postulated and studied as electron acceptors, resulting in surface conductivity even at very low concentrations [4]. In our previous study, we hypothesized that NO_2^- and/or O_3 may be responsible for the pseudo p-type doping observed on these H-MND [11]. However, these species would not participate in the C1s signature of the H-MND shallow surface. Focusing on carbon-based adsorbates involved in charge transfer doping, in their pioneering works during the 2000's [50,51], Maier, Ristein and co-workers mentioned HCO_3^- anions originating from CO_2 dissolved in the adsorbed water layer at the diamond surface. They proposed that HCO_3^- anions could be present at the diamond surface to compensate for the positive charge of the h^+ layer. Nevertheless, according to the NIST database and literature[52], C1s signature of HCO_3 anions adsorbed on thin film oxides should be located at binding energies ranging from 289 to 292 eV vs E_F. Here is the limit of this hypothesis, as we lack information on the binding energies of such anions adsorbed on nanodiamonds or nanocarbons, referenced to E_{VAC}.

Another possibility concerns the presence of adventitious carbon at the surface of MND. Thanks to the use of a nanoparticle jet directly formed from the colloid, the usual contamination occurring during the exposure of drop-casted particles to ambient atmosphere all along their preparation and storage is avoided here. However, when preparing the colloid, the nanoparticles were necessarily exposed to air between the time they left the oven in which they were oxidized or hydrogenated and the time they were introduced into the ultrapure water before sonication. Under our experimental conditions, this exposure to ambient air lasts a few hours up to a few days at maximum, during which we cannot exclude that a small amount of adventitious carbon is deposited at the surface of the powder. In 2017, Greczynski et al. [53] studied this adventitious carbon on different types of thin-films (metal, nitride, carbide, boride, oxide, and oxynitride) and measured a constant binding energy of 289.6 eV vs E_{VAC} whatever the substrate [54]. Considering our C1s spectra, this binding energy seems a little bit lower than C-O and C=O components. Thus, if we cannot exclude a contribution of this incidental carbon, it would remain limited and it does not prevent anyway the demonstration of negative electronic affinity (NEA) on H-MND and positive one (PEA) for Ox-MND.

Conclusion

A better knowledge of the shallow surface of nanodiamond is required to deeply understand its unusual colloidal properties and reactivity under illumination (radiolysis, H_2 production by water-splitting, etc.). The present study reported on synchrotron X-ray photoemission measurements performed on isolated (or slightly aggregated) ND in aerodynamic jet. In our experimental conditions (a photon energy of 360 eV), the probed depth was 0.3 nm. Using this original configuration, possible charging effects linked to the substrate or in situ modifications of ND under the photon incident beam can be excluded. Firstly, synchrotron XPS data allowed us to build band diagrams for oxidized and hydrogenated

View Article Online
DOI: 10.1039/D5NR02241J

milled nanodiamonds (Ox-MND and H-MND). As expected, a negative electron affinity (NEA) was obtained for H-MND whereas the affinity turned positive for Ox-MND. Such behaviors are the fingerprint of well-controlled diamond terminations as shown by the literature. Surprisingly, Ox-MND and H-MND exhibited quite similar C1s and O1s core level signatures, with exalted oxidized contributions compared to conventional XPS (close to 40% of the C1s area). If it was rather expected for Ox-MND, it was intriguing for the hydrogenated surface, which evidences NEA at the same time. As a possibility to explain this contradiction, we postulated either on a different spatial location of C-O bonds at both MND surfaces, on the role of an adsorbed water layer remaining on H-MND or on the presence of carbon-based adsorbates on the H-MND surface. The hypothesis of HCO_3^- adsorbates, which may be implied in the charge transfer doping observed on these H-MND, was discussed. The contribution of adventitious carbon cannot be completely excluded as well.

Whatever the origin of these unexpected XPS C1s signatures, synchrotron X-ray photoemission performed on these isolated particles in a jet revealed that hydrogenated and oxidized milled nanodiamonds finally exhibit very similar shallow surface chemistries, despite exhibiting opposite electron affinities. This raises questions of the true interface formed with water molecules when MNDs are dispersed in aqueous suspension, particularly in light of the growing body of research on their use as strong reductive photocatalysts.

4. Methods

Materials

Milled nanodiamonds SYP 0–0.05 (purity >99.9%) were acquired from Van Moppes (Switzerland).

ND preparation

Oxidized (Ox-MND) and hydrogenated (H-MND) nanodiamond colloids were prepared following the procedure detailed here[10]. In summary, oxidation was conducted by annealing as-received MND (300 mg) at 480°C for 5h under air at atmospheric pressure. For hydrogenation, 150 mg of Ox-MND were annealed at 750°C under pure H_2 with a flow of 50 sccm at atmospheric pressure. Then, 100 mg of treated powder were sonicated for 30 min in 2.5 mL of ultrapure water (18.2 MΩ.cm) using a Cup Horn Bioblock Scientific 750 W system, equipped with a cooling system. After a final centrifugation step (40 min at 2400 g), colloids of H-MND and Ox-MND are collected and their concentration is measured by weighing the residue of a known volume dried overnight at room temperature.

Infrared spectroscopy

IR spectra of all samples were acquired on a Bruker Alpha II spectrometer, with 2 µL of suspension drop-casted and dried under N_2 on the Platinum ATR system. They reveal the characteristic signatures of oxidized and hydrogenated surfaces with C=O and C-H stretching modes, respectively (Figure 9). For more details, please refer to our previous studies[10,18].

View Article Online
DOI: 10.1039/D5NR02241J

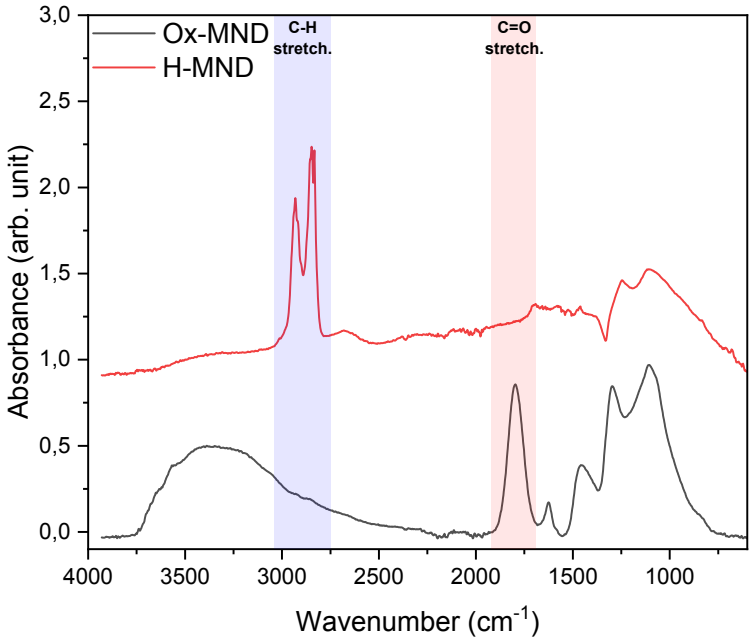

Figure 9 : IR spectra of H-MND and Ox-MND.

Conventional XPS

The XPS analyses presented here, conducted using a conventional laboratory spectrometer, are derived from our previous study on the same nanoparticles [10]. Briefly, ND were drop-casted on a silicon substrate covered with a gold coating. Measurements were performed on a Kratos Analytical Axis Ultra DLD spectrometer equipped with a monochromated Al Kα (1486.6 eV) X-ray source and a charge compensation system (Manchester, UK). C 1s spectra shown in this study were acquired at 10 eV of pass-energy to reach a higher energy resolution. Binding energies were referenced to the $Au_{4f7/2}$ peak located at 84 eV.

Jet of nanodiamonds and synchrotron XAPS

An aerosol flow composed of an Ar inert carrier gas and the sample in micro-droplet form is produced by atomization of a suspension of nanoparticles, using a commercial aerosol generator Palas AGK 2000. The droplets are then dried with a double-stage silica-gel dryer from TSI. The aerosol containing dried particles is then driven to an aerodynamic lens system that produces a focused, continuously renewable, nanoparticle beam under vacuum from the aerosol stream at atmospheric pressure. This is achieved by carrying the nano-aerosol flow through a 200 µm limiting entrance orifice, followed by a series of four compartments separated by diaphragms. The geometry of the system is identical to the design previously used on PLEIADES beamline[26,45]. It is part of a dedicated multipurpose source chamber and the system for X-ray aerosol photoelectron spectroscopy (XAPS)[45] available on the PLEIADES beamline at the French national synchrotron radiation facility SOLEIL.

The nanoparticle beam passes entirely through a 1.5 mm diameter skimmer and emerges into a high vacuum region before crossing the soft X-ray beam. The pressure in the interaction chamber is maintained at around 1×10^{-6} mbar. The beam of isolated nanoparticles crosses the synchrotron radiation beam, so that the interaction region between a nanoparticle and soft X-ray photons is well defined spatially. It should be noted that the focused NP beam allows to distinguish between the XPS signal related to the photoionization of NPs from the one originating from small atoms/molecules such as carrier gas, residual solvent or the gas introduced for calibration[45].

View Article Online
DOI: 10.1039/D5NR02241J

The XPS spectra were recorded using a wide-angle lens VG-Scienta R4000 electron energy analyzer, at several different photon energies, depending on a desired ionization energy (valence or inner shell). The photon beam was produced by a permanent magnet APPLE II type undulator with 80 mm period and monochromatized by using the modified Petersen plane grating monochromator and a high-flux 600 L/mm grating. For the photon energy calibration, the calibration gas was introduced into the calibration chamber (downstream to the XPS measurements) by an effusive jet crossing at the right angle of the SR beam and photo-ions were extracted and detected by a single channel multiplier ("Dr. Sjuts Optotechnik GmbH") connected to pulse counting electronics. The overall accuracy of the photon energy calibration in the whole energy range was estimated to be 0.2 eV, not including the accuracy of the literature values used as reference points.

For the photon energies used of 100 eV, 360 eV and 580 eV, the overall resolution in the XPS spectra was 0.11, 0.39, and 0.77 eV, respectively. The linearity of the photoelectron kinetic energy scale has been calibrated according to the 2p Ar IPs[55] measured by a Scienta XPS spectrometer under the same experimental conditions. The binding energy (BE) scale with respect to the vacuum level of each particular recorded XPS spectrum was calibrated according to a closely lying XPS line that corresponds to the ionization energy (IE) of an appropriate reference gas. The valence region was calibrated with respect to the ionization energy of water at 12.62 eV (from NIST Chemistry Webbook). The C1s XPS spectra were calibrated according to the CO_2 C1s IP at 297.7 eV [31]. Note that an uncertainty the incident photon energy does not influence the calibration of the binding energy scale, which only depends on the uncertainty in the linearity of the photoelectron kinetic energy scale and the error of the reference value. The residual water molecules from the solvent are always present in the interaction region, while calibrant gases (Ar and CO_2) are introduced in the chamber through a side leak. The overall uncertainty of BE due to the calibration is estimated to be 0.1−0.2 eV.

Acknowledgments

The experiments have been performed at the PLEIADES beamline at the SOLEIL Synchrotron, France (Proposal No. 20201236 and 20220294). We thank SOLEIL staff for the expert operation of the equipment and the storage ring during the experiments. Authors also acknowledge J. Leroy from NIMBE for conventional XPS measurements and CEA for funding M. Finas and L. Saoudi PhDs.

References

1 H. Wang and Y. Cui, *Carbon Energy*, 2019, **1**, 13–18.

2 Y. Wu and T. Weil, *Adv. Sci.*, 2022, **9**, 1–19.

3 K. P. Loh, D. Ho, G. N. C. Chiu, D. T. Leong, G. Pastorin and E. K. Chow, *Adv. Mater.*, 2018, **30**, 1–21.

4 K. G. Crawford, I. Maini, D. A. Macdonald and D. A. J. Moran, *Prog. Surf. Sci.*, 2021, **96**, 100613.

5 D. Miliaieva, A. S. Djoumessi, J. Čermák, K. Kolářová, M. Schaal, F. Otto, E. Shagieva, O. Romanyuk, J. Pangrác, J. Kuliček, V. Nádaždy, S. Stehlik, A. Kromka, H. Hoppe and B. Rezek, *Nanoscale Adv.*, 2023, **5**, 4402–4414.

6 J. R. Christianson, D. Zhu, R. J. Hamers, J. R. Schmidt, R. Christianson, D. Zhu, R. J. Hamers and J. R. Schmidt, *J. Phys. Chem. B*, 2013, **2**, 195–203.

7 L. Zhang and R. J. Hamers, *Diam. Relat. Mater.*, 2017, **78**, 24–30.

8 W. A. Maza, V. M. Breslin, T. I. Feygelson, P. A. DeSario, B. B. Pate, J. C. Owrutsky and A. Epshteyn, *Appl. Catal. B Environ.*, 2023, **325**, 122306.

9 G. Liu, C. Feng and P. Shao, *Environ. Sci. Technol.*, 2022, **56**, 6223–6231.

10 L. Saoudi, H. A. Girard, E. Larquet, M. Mermoux, J. Leroy and J. C. Arnault, *Carbon N. Y.*, 2023, **202**, 438–449.

11 C. Njel, H. A. Girard, M. Frégnaux, D. Aureau and J.-C. Arnault, *Carbon N. Y.*, 2024, **230**, 119668.

12 S. Stehlik, O. Szabo, E. Shagieva, D. Miliaieva, A. Kromka, Z. Nemeckova, J. Henych, J. Kozempel, E. Ekimov and B. Rezek, *Carbon Trends*, 2024, **14**, 100327.

13 J. C. Arnault and H. A. Girard, *Curr. Opin. Solid State Mater. Sci.*, 2017, **21**, 10–16.

14 T. Petit, L. Puskar, T. Dolenko, S. Choudhury, E. Ritter, S. Burikov, K. Laptinskiy, Q. Brzustowski, U. Schade, H. Yuzawa, M. Nagasaka, N. Kosugi, M. Kurzyp, A. Venerosy, H. Girard, J.-C. Arnault, E. Osawa, N. Nunn, O. Shenderova and E. F. Aziz, *J. Phys. Chem. C*, 2017, **121**, 5185–5194.

15 K. A. Laptinskiy, A. N. Bokarev, S. A. Dolenko, I. L. Plastun, O. E. Sarmanova, O. A. Shenderova and T. A. Dolenko, *J. Raman Spectrosc.*, 2019, **50**, 387–395.

16 M. Kurzyp, H. A. Girard, Y. Cheref, E. Brun, C. Sicard-Roselli, S. Saada and J.-C. Arnault, *Chem. Commun.*, 2017, **53**, 1237–1240.

17 E. Brun, H. A. Girard, J. C. Arnault, M. Mermoux and C. Sicard-Roselli, *Carbon N. Y.*, 2020, **162**, 510–518.

18 F. Ducrozet, E. Brun, H. A. Girard, J. C. Arnault and C. Sicard-Roselli, *J. Phys. Chem. C*, 2023, **127**, 19544–19553.

19 C. Marchal, L. Saoudi, H. A. Girard, V. Keller and J. Arnault, *Adv. Energy Sustain. Res.*, 2024, **5**, 1–8.

20 J. C. Arnault, *Diam. Relat. Mater.*, 2018, **84**, 157–168.

21 D. R. Baer and M. H. Engelhard, *J. Electron Spectros. Relat. Phenomena*, 2010, **178–179**, 415–432.

22 A. G. Shard, J. Wang and S. J. Spencer, *Surf. Interface Anal.*, 2009, **41**, 541–548.

23 A. G. Shard, *J. Phys. Chem. C*, 2012, **116**, 16806–16813.

24 C. Saucedo, N. Rieders and R. J. Hamers, *Diam. Relat. Mater.*, 2025, 112011.

25 M. K. Kuntumalla, A. Chemin, M. Finas, H. A. Girard, S. Michaelson, T. Petit, J.-C. Arnault and A. Hoffman, *J. Phys. Chem. C*, 2024, **128**, 15573–15582.

26 F.-X. Ouf, P. Parent, C. Laffon, I. Marhaba, D. Ferry, B. Marcillaud, E. Antonsson, S. Benkoula, X.-J. Liu, C. Nicolas, E. Robert, M. Patanen, F.-A. Barreda, O. Sublemontier, A. Coppalle, J. Yon, F. Miserque, T. Mostefaoui, T. Z. Regier, J.-B. A. Mitchell and C. Miron, *Sci. Rep.*, 2016, **6**, 36495.

27 S. Benkoula, O. Sublemontier, M. Patanen, C. Nicolas, F. Sirotti, A. Naitabdi, F. Gaie-Levrel, E. Antonsson, D. Aureau, F.-X. Ouf, S.-I. Wada, A. Etcheberry, K. Ueda and C. Miron, *Sci. Rep.*, 2015, **5**, 15088.

28 R.-Q. Yan, M. Cao and Y.-D. Li, *Materials (Basel).*, 2022, **15**, 3315.

29 S. Tanuma, C. J. Powell and D. R. Penn, *Surf. Interface Anal.*, 2011, **43**, 689–713.

30 H. A. Girard and J.-C. Arnault, in *Novel Aspects of Diamond II*, eds. S. Mandal and N. Yang, Springer Nature Switzerland, Cham, 2024, vol. 149, pp. 47–76.

31 V. Myrseth, J. D. Bozek, E. Kukk, L. J. Sathre and T. D. Thomas, *J. Electron Spectros. Relat. Phenomena*, 2002, **122**, 57–63.

32 A. Kahn, *Mater. Horizons*, 2016, **3**, 7–10.

33 S. Kono, T. Kageura, Y. Hayashi, S. G. Ri, T. Teraji, D. Takeuchi, M. Ogura, H. Kodama, A. Sawabe, M. Inaba, A. Hiraiwa and H. Kawarada, *Diam. Relat. Mater.*, 2019, **93**, 105–130.

34 R. Graupner, J. Ristein and L. Ley, *Surf. Sci.*, 1994, **320**, 201–207.

35 O. Romanyuk, Š. Stehlík, J. Zemek, K. Aubrechtová Dragounová and A. Kromka, *Nanomaterials*, 2024, **14**, 590.

36 K. Kolarova, I. Bydzovska, O. Romanyuk, E. Shagieva, E. Ukraintsev, A. Kromka, B. Rezek and S. Stehlik, *Diam. Relat. Mater.*, 2023, **134**, 109754.

37 S. Stehlik, M. Mermoux, B. Schummer, O. Vanek, K. Kolarova, P. Stenclova, A. Vlk, M. Ledinsky, R. Pfeifer, O. Romanyuk, I. Gordeev, F. Roussel-Dherbey, Z. Nemeckova, J. Henych, P. Bezdicka, A. Kromka and B. Rezek, *J. Phys. Chem. C*, 2021, **125**, 5647–5669.

38 O. S. Kudryavtsev, R. H. Bagramov, A. M. Satanin, A. A. Shiryaev, O. I. Lebedev, A. M. Romshin, D. G. Pasternak, A. V. Nikolaev, V. P. Filonenko and I. I. Vlasov, *Nano Lett.*, 2022, **22**, 2589–2594.

39 E. Ekimov, A. A. Shiryaev, Y. Grigoriev, A. Averin, E. Shagieva, S. Stehlik and M. Kondrin, *Nanomaterials*, 2022, **12**, 1–22.

40 D. R. Baer, M. H. Engelhard, G. E. Johnson, J. Laskin, J. Lai, K. Mueller, P. Munusamy, S. Thevuthasan, H. Wang, N. Washton, A. Elder, B. L. Baisch, A. Karakoti, S. V. N. T. Kuchibhatla and D. Moon, *J. Vac. Sci. Technol. A Vacuum, Surfaces, Film.*, , DOI:10.1116/1.4818423.

41 M. Finas, H. A. Girard and J.-C. Arnault, *Nanoscale Adv.*, 2024, **6**, 5375–5387.

42 O. Sublemontier, C. Nicolas, D. Aureau, M. Patanen, H. Kintz, X. Liu, M.-A. Gaveau, J.-L. Le Garrec, E. Robert, F.-A. Barreda, A. Etcheberry, C. Reynaud, J. B. Mitchell and C. Miron, *J. Phys. Chem. Lett.*, 2014, **5**, 3399–3403.

43 A. Chemin, M. K. Kuntumalla, M. Brzhezinskaya, T. Petit and A. Hoffman, *Appl. Surf. Sci.*, 2024, **661**, 160082.

44 P. Wang, T. X. Carroll, T. D. Thomas, L. J. Sæthre and K. J. Børve, *J. Electron Spectros. Relat. Phenomena*, 2021, **251**, 147103.

45 D. Danilović, D. K. Božanić, R. Dojčilović, N. Vukmirović, P. Sapkota, I. Vukašinović, V. Djoković, J. Bozek, C. Nicolas, S. Ptasinska and A. R. Milosavljević, *J. Phys. Chem. C*, 2020, **124**, 23930–23937.

46 D. Cahen and A. Kahn, *Adv. Mater.*, 2003, **15**, 271–277.

47 O. Manelli, S. Corni and M. C. Righi, *J. Phys. Chem. C*, 2010, **114**, 7045–7053.

48 A. Laikhtman, A. Lafosse, Y. Le Coat, R. Azria and A. Hoffman, *Surf. Sci.*, 2004, **551**, 99–105.

49 R. Akhvlediani, S. Michaelson and A. Hoffman, *Surf. Sci.*, 2010, **604**, 2129–2138.

50 F. Maier, M. Riedel, B. Mantel, J. Ristein and L. Ley, *Phys. Rev. Lett.*, 2000, **85**, 3472–3475.

51 M. Riedel, J. Ristein and L. Ley, *Phys. Rev. B*, 2004, **69**, 125338.

52 C. Yang, F. Bebensee, J. Chen, X. Yu, A. Nefedov and C. Wöll, *ChemPhysChem*, 2017, **18**, 1874–1880.

53 G. Greczynski and L. Hultman, *ChemPhysChem*, 2017, **18**, 1507–1512.

54 G. Greczynski and L. Hultman, *Appl. Surf. Sci.*, 2018, **451**, 99–103.

55 Thompson, A. Thompson, D. Attwood, E. Gullikson, M. Howells, K.-J. Kim, J. Kirz, J. Kortright, I. Lindau, Y. Liu, P. Pianetta, A. Robinson, J. Scofield, J. Underwood, G. Williams and H. Winick, *Lawrence Berkeley Natl. Lab.*, 2009, 176.

Data Availability Statement

View Article Online
DOI: 10.1039/D5NR02241J

Due to the large volume of data collected at the synchrotron, the data will be provided upon request from the authors